processes

MDPI

Article

GPR-Based Active Tracing of Nano-Barium Titanate-Modified Cement Grout for Underground Grouting Detection

Xianqi Xu [1], Rongping Tang [2], Zongren Yin [1], Lixuan Wu [3,4,*] and Yuxiang Huo [3,4]

[1] Sinohydro Bureau 14 Co., Ltd., Kunming 650041, China; 18287914582@163.com (X.X.); 15187486465@163.com (Z.Y.)
[2] Banda Hydropower Project Construction Management Bureau, Huaneng Lancang River Upper Stream Hydropower Co., Ltd., Kunming 650041, China; s18288413538@163.com
[3] State Key Laboratory of Geohazard Prevention and Geoenvironment Protection, Chengdu 610059, China; huoyuxiang10@cdut.edu.cn
[4] College of Environment and Civil Engineering, Chengdu University of Technology, Chengdu 610059, China
* Correspondence: wlxm824@163.com

Abstract

Accurate identification of grout diffusion extents and reinforcement boundaries in deep-buried, water-rich, or complex underground engineering is critical for surrounding rock stabilization, seepage prevention, and overall engineering safety. However, due to the concealed nature of underground structures and the marginal dielectric contrast between conventional cement grout and surrounding saturated formations, traditional ground penetrating radar (GPR) detection is often severely hampered by weak reflection signals and poor interface identifiability. To address this critical engineering challenge, a novel active electromagnetic tracing strategy based on nano-barium titanate (BTO) high-dielectric admixtures was proposed to deliberately modulate the dielectric properties of cement grout and amplify the electromagnetic impedance mismatch at the grouting boundary. Cement grout systems with different BTO dosages (0%, 5%, and 10%) were systematically investigated through 24 h continuous time-lapse GPR experiments and finite-difference time-domain (FDTD)-based gprMax numerical simulations. The results indicate that nano-BTO significantly increases the initial dielectric constant of the grout from 22.14 (0% BTO) to 42.90 (5% BTO) and 49.70 (10% BTO). At the 24 h terminal node, the dielectric constants remain at 24.06 and 35.52 for the 5% and 10% BTO groups, maintaining notable increments of 43.90% and 112.44% over the pure cement group (16.72). Consequently, the enhanced dielectric constant of the grout significantly boosts the interface reflection intensity in physical experiments; compared to the pure cement control group, the reflection amplitudes of the 5% and 10% BTO groups exhibit initial enhancements of 36.66% and 46.21%, respectively, and maintain terminal enhancements of 40.54% and 51.00% at the 24 h node, effectively securing long-term boundary clarity in GPR profiles. Both numerical simulations and physical experiments quantitatively confirm this reflection enhancement, validating the feasibility of the active tracing strategy. This study provides a novel technical paradigm and theoretical foundation for the non-destructive boundary identification, diffusion monitoring, and quality evaluation of concealed grouting bodies under complex underground environments, effectively serving underground engineering safety and disaster prevention.

Keywords: ground penetrating radar (GPR); active electromagnetic tracing; underground engineering safety; grouting quality detection; nano-BTO; dielectric constant

Check for updates

Academic Editor: Chuanjin Yao

Received: 22 August 2026
Revised: 1 October 2026
Accepted: 16 October 2026
Published: 2 November 2026

Copyright: © 2026 by the authors. Licensee MDPI, Basel, Switzerland. This article is an open access article distributed under the terms and conditions of the Creative Commons Attribution (CC BY) license.

1. Introduction

The construction of deep underground tunnels and hydraulic tunnels frequently faces severe challenges from geological conditions such as high in situ stresses, water-rich strata, and saturated surrounding rock masses. In this context, grouting technology has become an indispensable and crucial measure for reinforcing fractured rock masses, sealing water inflows, and ensuring the long-term structural stability and construction safety of underground engineering [1–4]. However, due to the severe concealment and spatial complexity of underground rock-grout systems, the actual diffusion pathways, effective consolidation range, and reinforcement boundaries of the slurry underground are exceptionally difficult to observe directly [5]. Inadequate or defective grouting can easily induce major engineering hazards such as surrounding rock collapse, water inrush, and lining cracking, making rigorous grouting quality control a vital prerequisite for disaster prevention and safety assurance in underground works [6–8]. Traditional quality inspection methods, such as core drilling, are destructive, time-consuming, and limited to point-based sampling, failing to provide continuous spatial evaluation [9,10]. Acoustic detection and resistivity also have difficulties in signal interpretation in complex strata [11,12]. Ground Penetrating Radar (GPR), owing to its advantages of being non-destructive, rapid, efficient, and capable of providing high-resolution subsurface images [13], has been widely applied in tunnel lining inspection [14], tunnel grouting detection and other work [15–17]. Nevertheless, when detecting the diffusion boundaries of cement grout in deep or saturated rock masses, conventional GPR frequently faces severe technical limitations, such as weak reflection signals, severe high-frequency attenuation, and blurred interfaces due to the weak dielectric contrast between conventional cement slurry and water-bearing host rocks [18,19].

To overcome this detection dilemma, the core innovation of this study is to shift the detection regime from conventional passive sensing to an active electromagnetic tracing strategy. Rather than passively relying on the marginal dielectric differences in natural formations, this study proposes to deliberately modulate the electromagnetic properties of the grout from the material source by introducing high-dielectric-constant admixtures. Barium titanate (BTO) is a typical inorganic non-metallic ferroelectric nano-ceramic material [20] with a high dielectric constant and excellent ferroelectric properties, the relative permittivity of plasma-sprayed BTO coatings typically ranges from about 300 to 400 [21–24]. It has been successfully employed in the development of electromagnetic shielding materials [25,26], the modification of cementitious systems and the enhancement of overall material dielectric constant [27–31], its potential as an active electromagnetic tracer to deliberately manipulate the dielectric contrast at rock-grout interfaces for underground engineering detection remains unexplored. By uniformly dispersing nanoscale BTO into conventional cement slurry, the dielectric constant of the fluid can be significantly elevated. This effectively enlarges the electromagnetic impedance mismatch at the boundary between the grouting body and the surrounding host rock, thereby substantially amplifying GPR reflected wave energy and fulfilling the purpose of high-contrast active tracing.

Conventional GPR detection represents a ‘passive identification’ approach that is inherently constrained by the natural dielectric contrast between host rocks and standard cement, which exhibits distinct limitations in complex geological settings such as deep underground engineering, water-rich formations, saturated surrounding rock, and concealed grouting zones. To address this challenge, the active electromagnetic tracing strategy proposed in this study aims to deliberately manipulate the electromagnetic impedance mismatch from the material source, thereby providing a promising exploratory avenue and potential technical approach for grouting boundary identification, diffusion tracking, and quality evaluation in complex underground environments. In this study, a multi-scale framework combining physical experiments and numerical simulations was established.

High-frequency 2 GHz GPR testing combined with precise geometric physical constraints was employed to dynamically track the time-dependent evolution of the dielectric constant of nano-BTO modified grouts with different dosages (0%, 5%, and 10%) across a 24 h continuous hydration window. Furthermore, physical rock-grout interface reflection experiments, gprMax numerical simulations, and microstructural SEM characterizations were conducted to elucidate the dynamic electromagnetic response enhancement mechanism. The results demonstrate that the incorporation of 5% and 10% nano-BTO elevates the initial dielectric constant of the cement grout by 93.77% and 124.48%, respectively, while maintaining sustained reflection amplitude enhancements exceeding 40% and 51% at the 24 h terminal node. This study is intended to provide preliminary theoretical insights and methodological exploration for non-destructive grouting detection and safety monitoring in complex underground engineering.

2. Materials and Methods

2.1. Preparation of Barium Titanate Cement Grout Specimens

Nano-BTO powder (Baisi Chemical, Guangdong, China) with an average particle size of 100 nm was selected as the admixture. This size effectively preserves high permittivity while ensuring uniform dispersion, low agglomeration, and pore-filling within the cement matrix. Ordinary Portland cement (P.O 42.5) was adopted, and the water-to-cement ratio (W/C) was set to 0.5 to satisfy the flowability and strength requirements standard in rock grouting engineering. As an exploratory proof-of-concept study, BTO dosages were designed at 0% (control), 5%, and 10% by cement mass. This gradient was selected to establish a baseline and capture the progressive electromagnetic enhancement with increasing admixture content, while balancing slurry preparation feasibility. The BTO dosages (0%, 5%, and 10%) were determined based on the mass ratio of BTO to cement. A total of two groups were set up in the experiment, with each group containing three specimens. The composition proportions of the different specimens are shown in Table 1.

Table 1. Composition proportions of the three cement grout groups.

Specimen Number	W:C:BTO
A, D	1:2:0
B, E	1:2:0.1
C, F	1:2:0.2

During the preparation of the mixed cement grout, to achieve uniform dispersion of the nanomaterials as much as possible, the weighed BTO powder was first added to pure water and stirred at high speed using a mechanical stirrer to form a uniform suspension in the water and prevent it from settling during standing. Subsequently, the calibrated weight of Portland cement was slowly added to the suspension in batches, with continuous stirring until the grout was uniform and free of lumps. The batching and mechanical mixing procedures were conducted in strict accordance with the standard laboratory cement testing method (GB/T 17671-2021). The hardened specimens designated for 28-day microstructural characterization were cured in a standard curing cabinet at a temperature of 20 ± 1 °C and a relative humidity of not less than 90%, in compliance with GB/T 17671-2021.

For the subsequent GPR detection, two types of molds with distinct specifications were designed to meet specific testing requirements:

(1) Dielectric Constant Inversion Group (A, B, C): The prepared grout was poured into acrylic molds with dimensions of 150 × 100 × 50 mm. A hollow PPR pipe, with an outer diameter of 20 mm and a wall thickness of 2.8 mm, was pre-fixed horizontally at

the center of the mold with both ends sealed. The purpose of sealing the hollow PPR pipe was to prevent grout infiltration, thereby providing a reflection target at a known depth with a strong electromagnetic impedance contrast. This configuration facilitates the precise inversion of the grout's dielectric constant from GPR signals.

(2) Reflection Amplitude Analysis Group (D, E, F): Three groups of grout with the same mix proportions were prepared and poured into molds measuring 100 × 100 × 10 mm. A dry granite block of 100 × 100 × 50 mm was placed in close contact with the upper surface of the grout to simulate the interface between the rock mass and the grout. This setup was utilized to extract and investigate the reflection amplitude characteristics at the cement grout-rock interface. All specimens were placed in a constant-temperature laboratory environment for continuous detection.

2.2. Working Principle of Ground Penetrating Radar

GPR technology is a non-destructive high-frequency electromagnetic detection technique. Its working principle involves transmitting high-frequency, short-pulse electromagnetic waves into the subsurface via a surface transmitting antenna. When the wavefront encounters a dielectric interface with different dielectric constants along its propagation path, part of the electromagnetic wave's energy is reflected or scattered due to the difference in electromagnetic wave impedance. This reflected energy returns to the surface and is captured by the receiving antenna, while the remaining energy is transmitted and continues to propagate downwards. By comprehensively analyzing the two-way travel time, amplitude strength, phase variations, and spectral characteristics of the recorded reflection signals, the spatial position and geometric shape of the underground target can be quantitatively inferred [32–35].

In this study, an SIR-4000 system (GSSI, Nashua, NH, USA) equipped with a Model 62000 2 GHz Palm antenna was utilized. To eliminate errors arising from manual operation, such as trajectory deviation and non-uniform scanning velocity, the 2 GHz antenna was mounted on a customized GPR scanning auxiliary device. Driven by a stepper motor, this device guides the antenna along a predefined track for fixed-point, constant-velocity reciprocating movement. This setup ensures high consistency in spatial positioning and coupling conditions for each scan during the time-lapse monitoring process (see Figures 1 and 2).

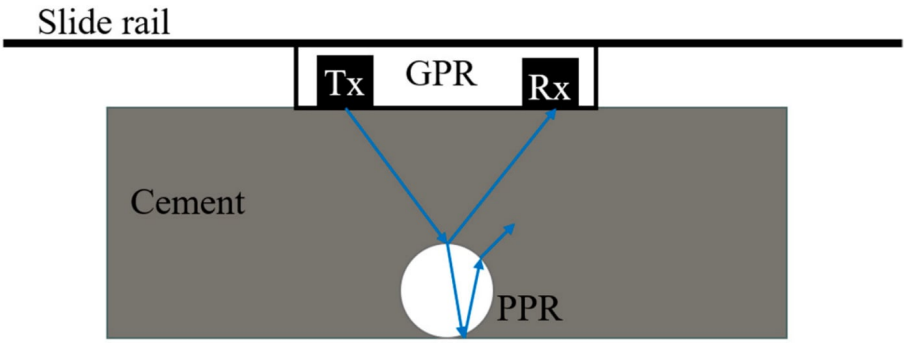


Figure 1. Schematic diagram of GPR operation.

2.3. Laboratory Continuous Scanning and Measurement Scheme

A time-lapse dynamic monitoring strategy was employed in the experiment, utilizing a motor to control the antenna along a slide rail for continuous, constant-velocity detection of the specimens (see Figure 3).

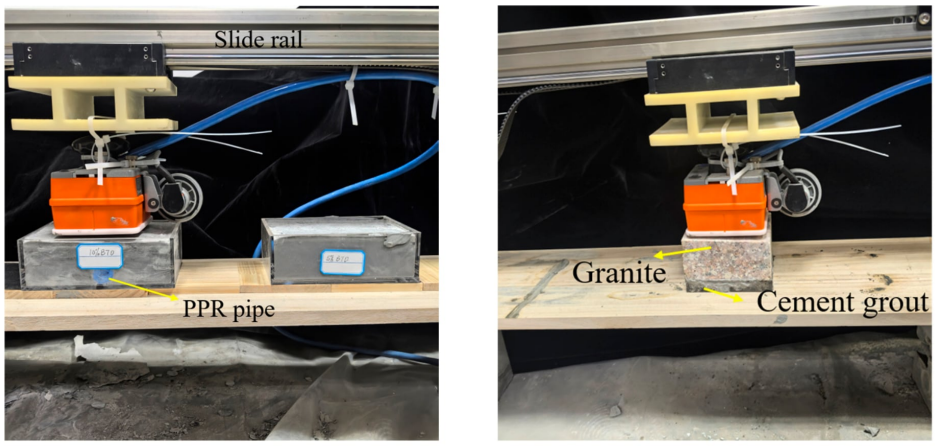
The experiment scanned six groups of specimens over a 24 h period at 10 min intervals to record in detail the evolution of the dielectric constant and interface reflection amplitude of each material group over hydration time. Each scan was set with fixed start and end

coordinates, and the antenna swept across the specimen surface from right to left at a constant velocity.



(**a**) (**b**)

Figure 2. Experimental equipment: (**a**) SIR-4000 GPR control unit; (**b**) 2 GHz antenna.



(**a**) (**b**)

Figure 3. GPR detection of cement grout using a 2 GHz antenna controlled by a slide rail: (**a**) Specimens A, B, and C for dielectric constant inversion; (**b**) Specimens D, E, and F for reflection amplitude analysis.

During GPR operation, the control unit records the double-travel time (two-way travel time) of the electromagnetic waves propagating through the cement grout. Based on this travel time and the known burial depth of the target, the wave velocity and dielectric constant of the medium can be derived, using the following equations [36,37].

$$v = \frac{C}{\sqrt{\varepsilon}} \quad (1)$$

$$\varepsilon = \left(\frac{CT}{2H}\right)^2 \quad (2)$$

where v represents the propagation velocity of electromagnetic waves in the medium; H is the burial depth of the target; C is the velocity of electromagnetic waves in a vacuum (0.3 m/ns); T denotes the double-travel time; and ε is the dielectric constant of the medium.

PPR material possesses a low dielectric constant (typically around 2) [38]. Given that the pipe is air-filled, it maintains a significant dielectric contrast with the early-stage unhardened cement grout [39]. This creates a pronounced electromagnetic impedance mismatch at the interface, which is expected to manifest as a distinct hyperbolic high-reflection coherent event in the GPR B-scan images. By extracting the double-travel time from the apex of this hyperbola, the dielectric constant of the grout can be calculated via Equation (2). Calibration tests using the same frequency band identified a dielectric constant of 4.8 for the dried granite used in this study.

2.4. Data Processing

Signal processing of the raw GPR profile was conducted using ReflexW (version 9.5) software following the sequential workflow illustrated in Figure 4: (1) Subtract-DC-Shift was applied to eliminate direct current baseline drift and system low-frequency bias; (2) Move Start Time (Time-zero correction) was performed to calibrate the ground-coupling surface and establish the true propagation time origin; (3) Energy Decay was implemented to compensate for spherical geometric spreading losses and high-frequency dissipation within the dissipative grout; (4) Subtracting Average (Background removal) was utilized to suppress horizontal direct waves and continuous ground clutter; (5) Bandpass Butterworth Filtering was adopted to isolate the effective 2 GHz spectrum and filter out high-frequency noise and low-frequency interference; and (6) Running Average was performed to enhance horizontal trace coherence and highlight the hyperbolic reflection events. The data from the six specimens across the two experimental groups were processed individually, and representative results are displayed in Figure 5.

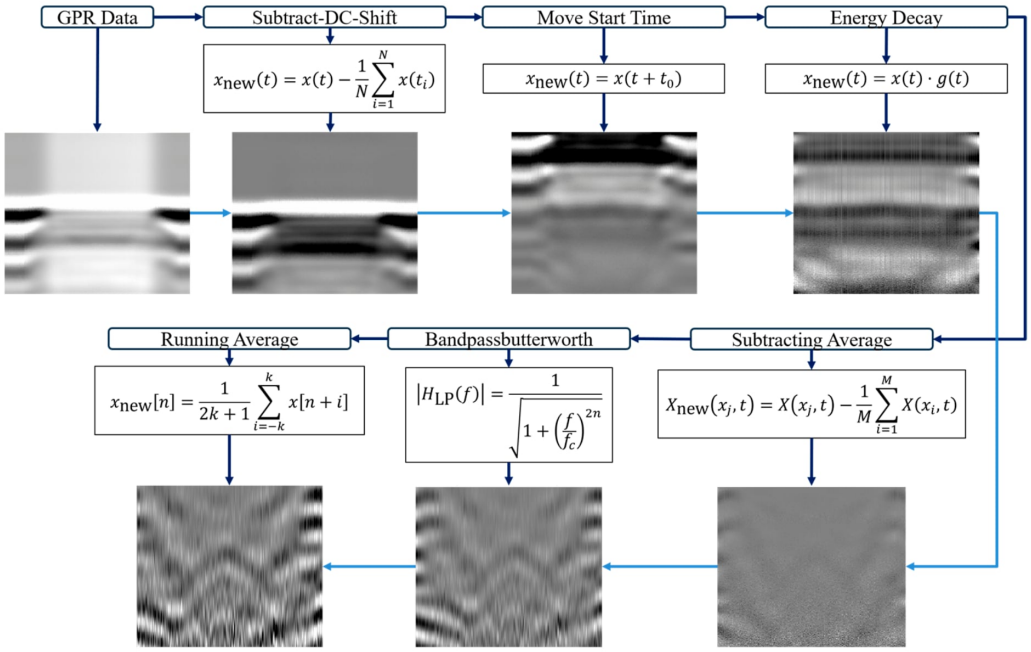


Figure 4. GPR data processing workflow implemented in ReflexW.

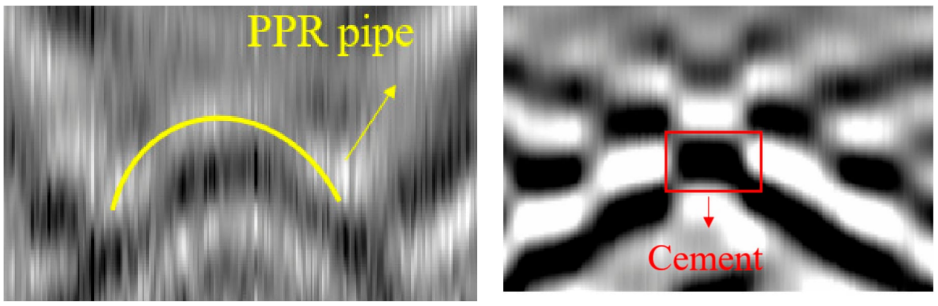


Figure 5. B-scan images of the experimental specimens: (**a**) Dielectric constant inversion group (Specimens A, B, and C); (**b**) Reflection amplitude analysis group (Specimens D, E, and F).

As shown in Figure 5a, the high free-water content and ion concentration within the cement grout lead to significant electromagnetic attenuation and polarization losses. Consequently, the high-frequency electromagnetic waves undergo intense scattering within the grout medium, resulting in a low signal-to-noise ratio (SNR) characterized by prominent

background noise. Despite the substantial dielectric contrast between the PPR pipe and the surrounding grout, the reflection interface of the PPR pipe manifests as a weak and severely attenuated diffraction hyperbola. This demonstrates the penetration limitations of high-frequency antennas in high-conductivity media.

Figure 5b presents the 2 GHz imaging results of the cement grout situated beneath the granite layer. In stark contrast to the highly dissipative grout medium, the overlying intact granite—acting as a low-dielectric-constant medium—significantly facilitates electromagnetic wave penetration with minimal high-frequency dispersion. This results in a profile with a clear background and high SNR, where the spatial morphology of the cement grout is vividly resolved as a high-amplitude diffraction hyperbola. These findings demonstrate the superior resolution capabilities of the 2 GHz antenna in homogeneous, low-attenuation media.

Following image processing, representative A-scans were extracted from the hyperbolic apices (Figure 6). In Figure 6a, a distinct positive peak (A_{PPR}) is observed due to the positive reflection coefficient from the grout to the air-filled PPR pipe, from which the two-way travel time is extracted to determine the grout's dielectric constant via Equation (2). In Figure 6b, a negative reflection trough (A_C) occurs due to phase reversal at the granite–grout interface, where the extracted amplitude directly quantifies the electromagnetic impedance mismatch to evaluate the active tracing enhancement.

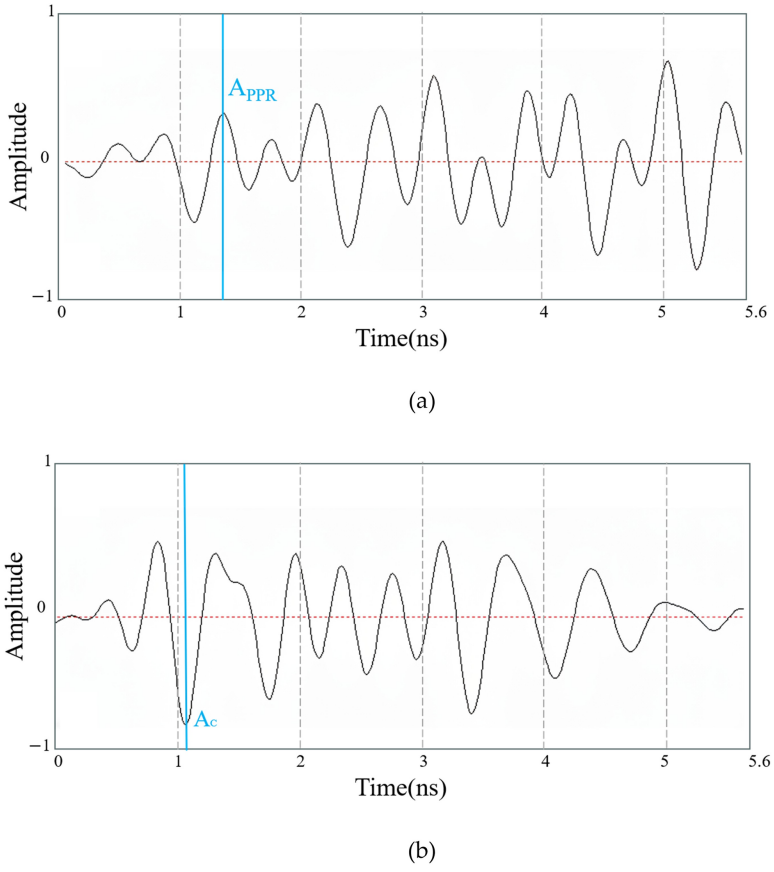


Figure 6. A-scan profiles extracted from the radar data: (**a**) A-scan at the apex of the PPR pipe; (**b**) A-scan at the granite–grout interface.

3. Results

3.1. Microstructural Morphology Analysis

To establish the microstructural basis for the dielectric characteristics and electromagnetic responses of the modified grout, the fracture surface morphology of the hardened

BTO-modified cement grout after 28 days of standard curing was characterized. Figure 7 presents representative SEM images for the 5% and 10% BTO dosage groups.

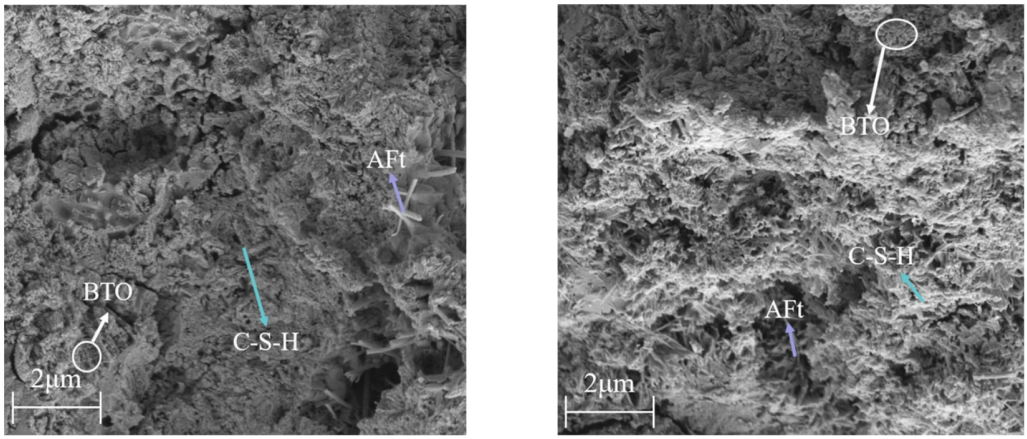


Figure 7. SEM images of hardened BTO-modified cement grout after 28 days of curing: (**a**) 5% BTO; (**b**) 10% BTO.

For the grout with 5% BTO, the matrix consists of interlocked flocculent and foil-like C-S-H gels alongside needle-like ettringite crystals, with the surfaces of residual dense particles tightly encapsulated by hydration products. The fine-particle phases are uniformly distributed within the hydrated matrix, and no obvious large-scale agglomerates are observed in the field of view. This uniform dispersion maximizes the interfacial contact area between the nano-BTO particles and the cement matrix, thereby providing abundant polarization sites.

For the grout with 10% BTO, the interlocking structure formed by ettringite crystals and C-S-H gels becomes denser, with a greater number of fine particles observed adhering to the crystal surfaces and filling the intercrystalline pores. This indicates that a larger amount of nano-BTO particles is incorporated into the hydrated matrix while maintaining favorable dispersion. Furthermore, the fine BTO particles attached to the surfaces of cement grains and hydration products can hinder the diffusion of water toward the unhydrated particle cores, providing direct microstructural evidence for the retarding effect of BTO on cement hydration.

3.2. Dynamic Evolution Law of Dielectric Constant

3.2.1. Inversion and Evolution Characteristics of Dielectric Constant

The double-travel time from the base of the 2 GHz antenna to the PPR pipe was determined by extracting the time (in nanoseconds) at the positive wave peak. The dielectric constant of the cement grout was subsequently calculated using Equation (2). Figure 8 illustrates the temporal evolution of the dielectric constants for specimens A, B, and C, while the corresponding fitting equations are summarized in Table 2.

Table 2. Fitting equations for the dielectric constant.

Specimen Number	Fitting Equation	R^2
A	$y = 32.24201 - 6.35285x^{0.12643}$	0.87179
B	$y = 43.6948 - 0.00881x^{1.07153}$	0.97118
C	$y = 50.05915 - 2.14522 \times 10^{-4}x^{1.53892}$	0.95904

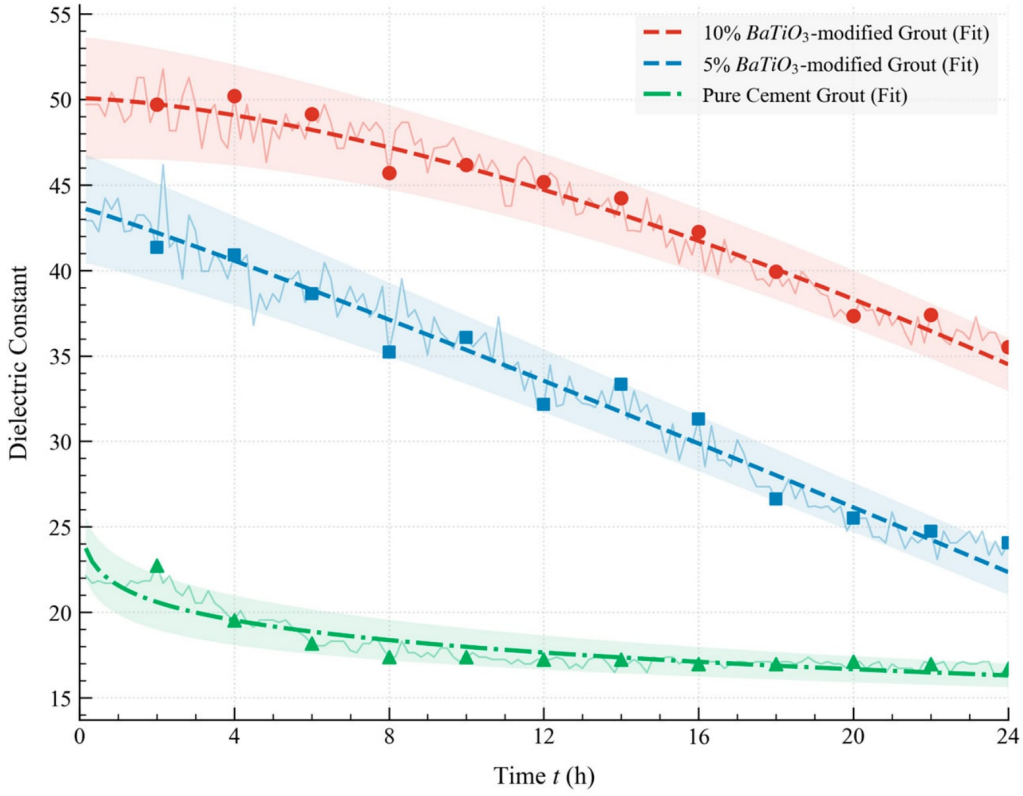


Figure 8. Variation curves of the dielectric constant. Note: Solid markers (circles for 10% BTO, squares for 5% BTO, and triangles for Pure Cement) represent the discrete experimental inversion values sampled at 2 h intervals; the faint fluctuations in the background indicate the continuous 10 min time-lapse data; bold lines represent non-linear fitting curves; and the shaded areas denote 95% confidence bands.

Figure 8 presents the quantitative inversion of the dynamic evolution of the dielectric constant for the three specimens over a 1440 min duration. Overall, all specimens exhibited a monotonic decreasing trend in dielectric constant over time. This attenuation in macro-electromagnetic properties is fundamentally governed by the hydration process of the cement. During the initial stage of hydration, the grout contains a large volume of free water molecules characterized by a high dielectric constant. As the reaction progresses, these free water molecules are gradually consumed and converted into chemically bound water or physically adsorbed water within the calcium silicate hydrate (C-S-H) gel and other hydration products. This microstructural transformation manifests macroscopically as a continuous decline in the system's dielectric constant. Notably, in preliminary trial measurements, intermediate dosages of 2% and 3% nano-BTO were also tested; their dielectric constant evolutions exhibited a steady, monotonic transition consistent with the overall trend between the 0% and 5% groups. To establish a focused comparative baseline, the main manuscript highlights the representative 0%, 5%, and 10% gradients.

A comparative analysis of the data for A, B, and C reveals that the incorporation of BTO significantly influences both the initial dielectric constant and its evolutionary trajectory. For the pure cement grout (Specimen A), the initial dielectric constant was 22.14—primarily contributed by free water—which rapidly decayed and stabilized at approximately 17 after 120 min. This indicates that the Portland cement underwent rapid early-stage hydration before transitioning into a diffusion-controlled phase. As a typical inorganic non-metallic ferroelectric nano-ceramic material, the dispersion of BTO particles is equivalent to introducing additional electric dipole moments into the cement grout system. Upon the addition of 5% (Specimen B) and 10% (Specimen C) BTO, the initial dielectric constants of the systems

increased to 42.9 and 49.7, respectively. This abrupt increase in the dielectric constant suggests that under a 2 GHz high-frequency alternating electromagnetic field, the macroscopic dielectric response of the BTO-modified grout is dominated by the spontaneous polarization of BTO particles and the interfacial polarization formed between the BTO particles and the cement matrix. Over the 1440 min observation window, the dielectric constant curves for Specimens B and C maintained a continuous monotonic decline without showing signs of reaching a steady state. This indicates that the introduction of nano-BTO materials exerts a significant retarding effect on the hydration process of the cement grout. The BTO particles act as barriers, obstructing the diffusion of water toward the surfaces of unhydrated cement particles. Consequently, the consumption rate of free water is substantially reduced, significantly extending the conversion period from free water to chemically bound water. This is reflected macroscopically as a sustained and gradual decline in the dielectric constant throughout the 1440 min period.

The fitting curves in Table 2 clearly demonstrate that BTO doping alters the dielectric constant attenuation characteristics of the cement grout. Specimen A follows a typical exponential decay model. During the first 400 min of hydration, the rapid conversion of free water to bound water causes a sharp decrease in the dielectric constant, after which the curve quickly converges and levels off. This transition marks the conclusion of the intensive early-stage hydration, as the system enters a stable microstructural phase dominated by ion diffusion.

In contrast, the fitting curves for Specimens B and C exhibit a significant increase in the *y*-axis intercept (initial dielectric constant), and the geometric configuration of their attenuation trajectories undergoes an inversion—shifting from rapid convergence to a sustained decline; the fitting curves for Specimens B and C maintain a stable negative slope without reaching convergence. This reflects the retarding effect of BTO nanomaterials on the early hydration of the cement matrix.

3.2.2. Multi-Time Window Variance Analysis of Dielectric Constant

To further quantify the impact of incorporating nano-BTO on the cement hydration process, sample variance was introduced to statistically evaluate the dispersion of dielectric constants across the four temporal windows: 0–120 min, 120–400 min, 400–1200 min, and 1200–1440 min. The results indicate that the evolutionary trajectory of the system's dielectric constant aligns well with the underlying hydration mechanisms (see Table 3).

Table 3. Sample variance of the relative dielectric constant (ε) for Specimens A, B, and C across different hydration intervals.

Sample Variance	A	B	C
0–120 min	0.108	0.706	0.771
120–400 min	1.364	3.768	1.669
400–1200 min	0.153	16.159	11.350
1200–1440 min	0.073	0.451	0.644

For the pure cement grout (Specimen A), the variance during the initial 0–120 min was merely 0.108, indicating a relatively stable free water content prior to large-scale phase conversion. However, during the 120–400 min interval, this variance increased to 1.364, corresponding to the intense hydration phase where free water is rapidly consumed and converted into physically adsorbed and chemically bound water. In contrast, the variances of the modified grout groups (Specimens B and C) during the 0–120 min phase had already risen to 0.706 and 0.771, respectively, and remained at elevated levels (3.768 and 1.669) throughout the 120–400 min window. This early increase in data dispersion confirms

that nano-BTO directly influences the initial flocculation structure and the corresponding electromagnetic response of the grout.

The prolonged 400–1200 min window exhibited the most significant inter-group discrepancies. The variance of Specimen A sharply decreased to 0.153, marking the completion of the early intense hydration phase. The pure cement system then transitioned into a microstructure stabilization period dominated by ion diffusion, wherein the macroscopic dielectric constant exhibited a convergent state with minimal fluctuation. Conversely, the variances for Specimens B and C reached their global peaks of 16.159 and 11.350, respectively, during this same period.

Towards the end of the 24 h monitoring period, the variance of Specimen A was marginal (0.073), indicating that changes in the dielectric constant had largely stagnated. Although the variances of Specimens B (0.451) and C (0.644) experienced a substantial decline from the previous stage, these remaining non-zero values suggest that during the final testing phase, a subtle yet continuous hydration dynamic persists within the BTO-incorporated systems, which have not yet reached a final electromagnetic steady state.

3.3. Amplitude Analysis of Physical Experiments

For specimens D, E, and F, the negative peak amplitude values at the reflection interface were extracted [40,41], as illustrated in Figure 6b. To minimize random errors associated with manual selection in the software, the six data points collected within each hour were averaged to represent the hourly amplitude. A total of 24 hourly amplitude values were recorded over the 24 h monitoring period, with the final statistical results presented in Figure 9.

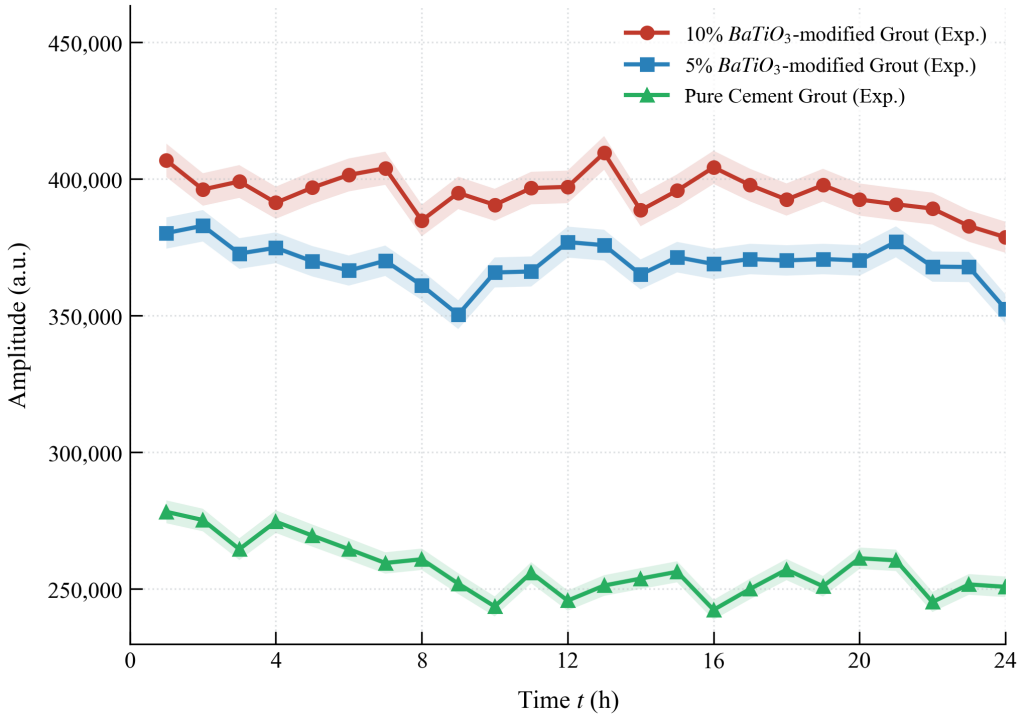


Figure 9. Statistical plot of reflection amplitudes from physical experiments.

Based on the 24 h continuous detection data shown in Figure 9, the reflection amplitude of electromagnetic waves at the granite-cement grout interface exhibits significant numerical differences depending on the BTO dosage. For the pure cement grout without BTO (Specimen D), the interface reflection amplitude remained at the lowest level throughout the monitoring cycle. Upon adding 5% BTO (Specimen E), a marked increase

in reflection amplitude was observed. When the BTO dosage was further increased to 10% (Specimen F), the interface reflection amplitude reached the highest level among the three experimental groups. This positive correlation demonstrates that the incorporation of nano-BTO materials effectively enhances the reflection intensity of the target interface in GPR images. From the perspective of electromagnetic wave propagation mechanisms, this amplitude enhancement effect is attributed to the superior dielectric properties of the BTO nanomaterials. As indicated by the inversion results in Section 3.1, the dispersion of BTO as a ferroelectric nano-ceramic material significantly elevates the overall dielectric constant of the mixed grout. Since the overlying dry granite is a low-dielectric-constant medium, a substantial electromagnetic impedance mismatch occurs when high-frequency electromagnetic waves transmit downward from the granite into the high-dielectric-constant cement grout. According to the laws of electromagnetic reflection, a greater disparity in the dielectric constant between the media on either side of an interface results in stronger reflected energy. Consequently, the increased BTO dosage amplifies the dielectric contrast at the rock-grout interface, manifesting macroscopically as a significant increase in the interface reflection amplitude. These results confirm the feasibility of an active tracing strategy that utilizes high-dielectric admixture to achieve visualization enhancement of the grouting zone in radar images.

Furthermore, observations of the dynamic amplitude evolution over time reveal that the interface amplitude curves for all three specimens remained relatively stable throughout the 24 h test period, with a slight downward trend emerging only after 20 h and no signs of abrupt attenuation. Although the analysis in Section 3.1 indicates that the conversion of free water to bound water during cement hydration leads to a monotonic decline in the grout's dielectric constant, the retarding effect of BTO nanomaterials on the early hydration process reduces the consumption rate of free water. As a result, the dielectric constant of the BTO-modified grout remains at a significantly higher level compared to the overlying granite over the 24 h period. This sustained and stable electromagnetic impedance difference ensures high signal-to-noise ratios and distinct identifiability of the grouting interface over extended periods, providing a sufficient time window for non-destructive GPR inspections in concealed underground engineering environments.

3.4. Amplitude Analysis via Numerical Simulation

This study further employed the gprMax3.0 software, based on the Finite-Difference Time-Domain (FDTD) algorithm [42,43], to construct an idealized 3D model of the granite-cement grout system. This approach serves to theoretically validate the physical experimental phenomena and provide mechanistic insights. The specific model parameters are detailed in Table 4.

Table 4. Parameters for the Numerical Model.

Parameter	Value
Domain size/m	0.6 × 0.1 × 0.6
Grid size/m	0.002 × 0.002 × 0.002
Waveform type	Ricker
Center frequency/MHz	2000
Antenna step size/m	0.005
Time window/ns	3
Media	Granite, Cement grout

The dielectric constants in the model were configured based on empirical measurements: the granite was assigned a dielectric constant of 4.8 with a conductivity of 1×10^{-5} s/m, while the cement grout dielectric constant was set using the hourly averaged values (6 data points

per hour) with a conductivity of 0.5 s/m. The dimensions for both media were defined according to the actual physical experimental setup, as visualized in the 3D model in Figure 10. The representative simulation results are displayed in Figure 11, demonstrating high consistency between the numerical simulations and the physical experiments.

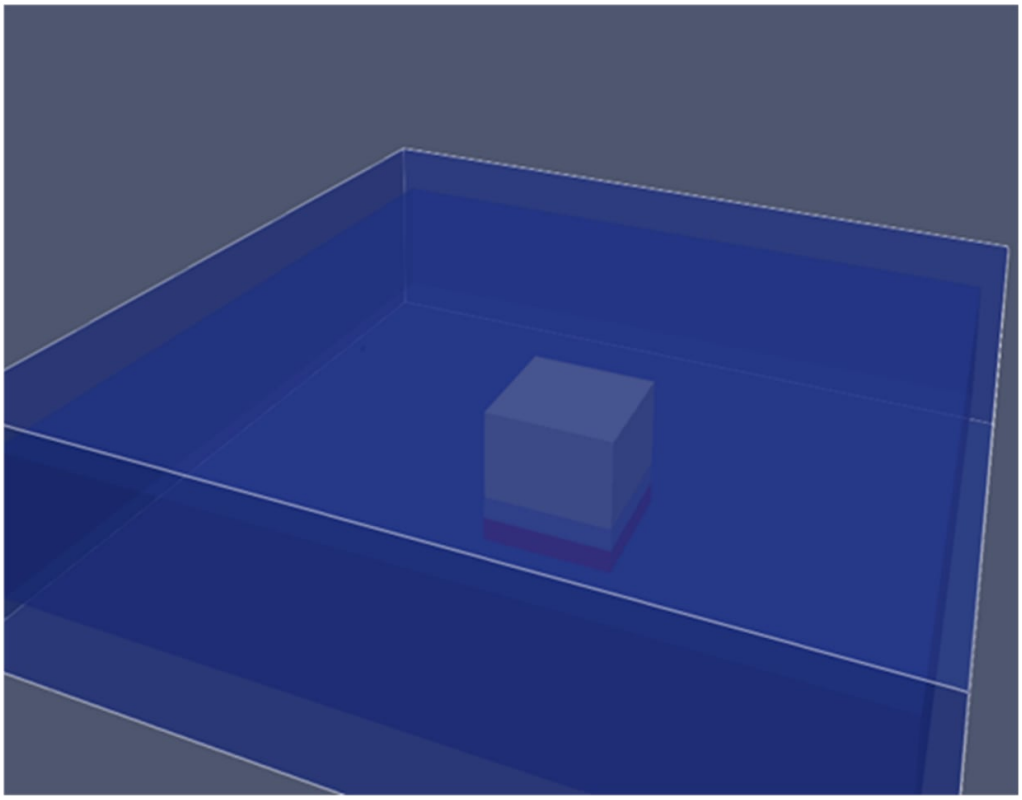


Figure 10. 3D numerical model of the granite-cement grout system.

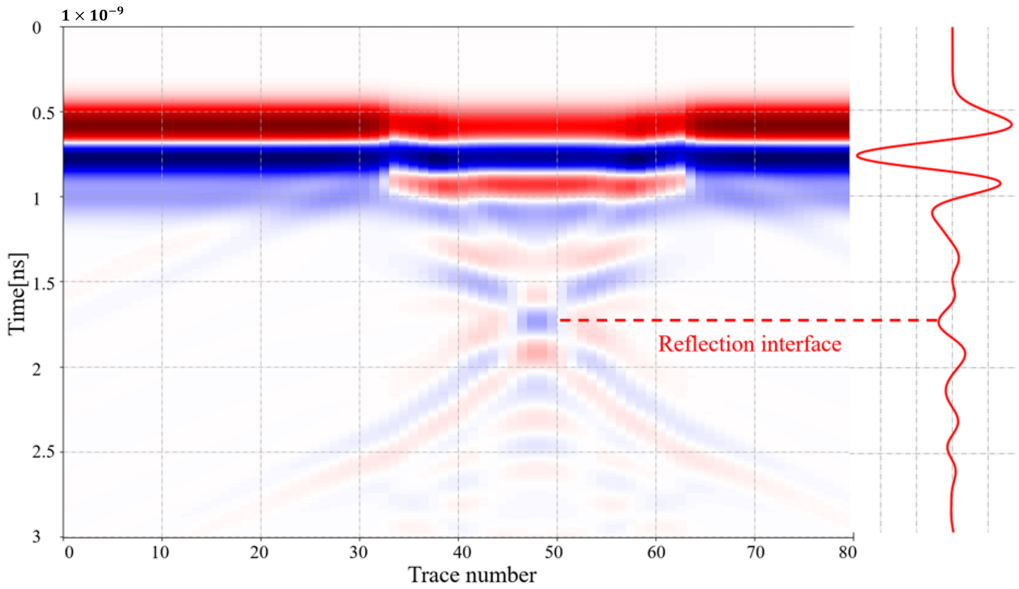


Figure 11. Results of the GPR numerical simulation.

Following the procedure shown in Figure 11, the A-scan from the 48th trace (center of the model) was extracted to determine the reflection amplitudes. The statistical results for the three experimental conditions are plotted in Figure 12.

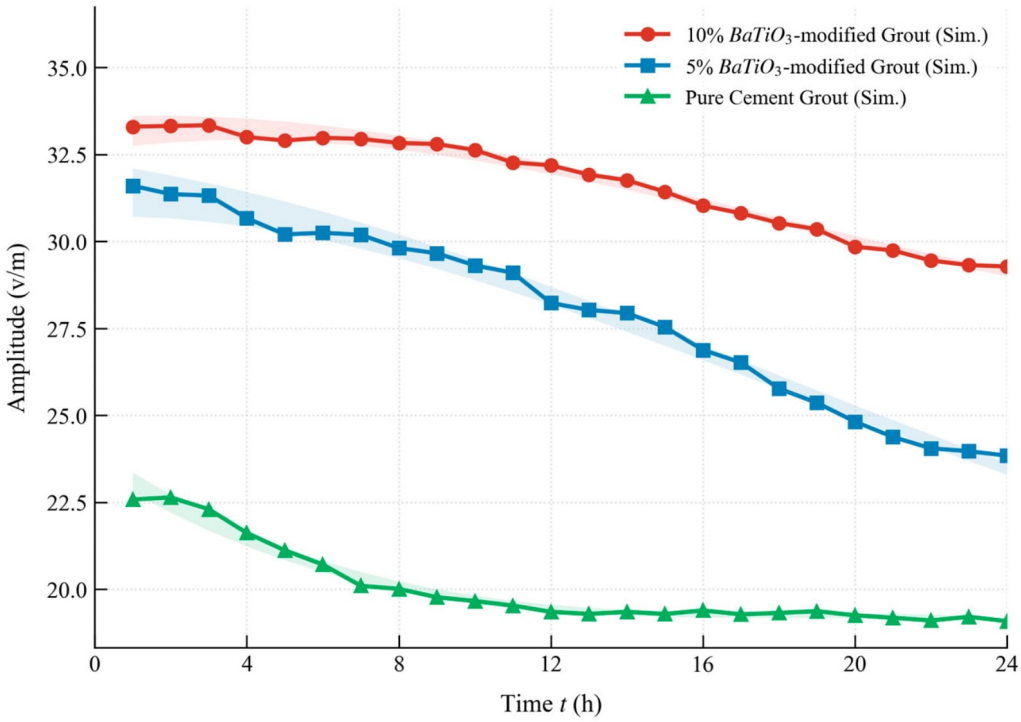


Figure 12. Statistical plot of reflection amplitudes from numerical simulations.

It should be noted that the reflection amplitudes in the physical experiments (Figure 9) and numerical simulations (Figure 12) have different metrics: the experimental values represent raw digitized signal amplitudes recorded by the GPR receiver in arbitrary units (a.u.), whereas the gprMax simulations output electric field intensity in V/m. Therefore, the comparison between them is aimed at evaluating relative response behaviors and macroscopic variation trends rather than matching absolute numerical magnitudes. From this perspective, the experimental data in Figure 9 and the gprMax simulation results in Figure 12 exhibit clear consistency in their response trends: specifically, an evident upward trend in interface reflection amplitude as the BTO dosage increases. However, discrepancies exist in the evolutionary patterns of these amplitudes. The numerical simulation curves in Figure 12 exhibit a steeper and more continuous decline, whereas the physical experimental curves in Figure 9 remain relatively stable with a reduced attenuation magnitude over the 24 h period.

This discrepancy primarily stems from two inherent assumptions and limitations in the gprMax numerical model. First, the model assumes a simplified homogeneous medium, whereas hydrating grout is a time-varying multiphase system. Under 2 GHz excitation, nano-BTO induces localized interfacial polarization that does not decay as rapidly as the bulk dielectric constant, mitigating amplitude attenuation in physical tests. Second, the model adopts a static electrical conductivity, whereas actual grout conductivity continuously declines with hydration due to free-water consumption and restricted ion migration; this reduced propagation loss partially compensates for reflection amplitude drop. To minimize these limitations, experimentally derived hourly dielectric constants were dynamically assigned to the grout domain, ensuring that macroscopic hydration kinetics were faithfully incorporated without relying on unconstrained multi-parameter fitting.

4. Discussion

The results demonstrate that nano-BTO can effectively regulate the electromagnetic response characteristics of cement grout. By increasing the initial dielectric constant of the

grout from 22.14 (0% BTO) to 42.9 (5% BTO, an increase of 93.77%) and 49.70 (10% BTO, an increase of 124.48%), nano-BTO enhances the electromagnetic impedance mismatch between the granite and the cement grout. This directly increases the interface reflection amplitude and improves boundary identifiability.

The dielectric constant inversion results indicate that BTO not only increases the initial dielectric constant of the grout but also alters its attenuation behavior during hydration. The early monotonic dielectric decline in pure cement agrees with previous findings [32,39], which demonstrated that rapid free-water consumption and bound-water formation lead to an electromagnetic plateau within 6–8 h. In contrast, BTO-modified grouts exhibited sustained dielectric decline over 24 h, eventually slowing down to terminal values of 24.06 (5% BTO) and 35.52 (10% BTO), maintaining a net dielectric superiority of 43.90% and 112.44% over the pure cement group (16.72). This difference is attributed to the retarding effect of BTO nanoparticles, which physically hinder moisture migration to unhydrated clinker cores and prolong free-water retention, thereby securing an extended high-contrast detection window. Variance analysis further confirms this mechanism, as modified grouts maintain active dielectric fluctuations over a prolonged duration (peaks of 16.159 and 11.350) while pure cement rapidly stabilizes.

Both the physical experiments and gprMax simulations verify the reflection enhancement effect of the BTO-modified grout. In the physical experiments, compared with the pure cement control group, the initial reflection amplitudes increased by 36.66% (5% BTO) and 46.21% (10% BTO), respectively. At the 24 h node, the amplitudes for the 5% and 10% BTO interfaces maintained high-level enhancements of 40.54% and 51.00% over the control group at the same time node. In comparison, the gprMax numerical simulations present a similar trend, where the initial simulated amplitude increases for the 5% and 10% dosages are 39.95% and 47.48%, respectively, and the simulated increases at the 24 h node are 24.95% and 53.46%, respectively. However, the amplitude attenuation trend in the numerical simulations is more idealized than that in the physical experiments. This discrepancy primarily stems from the fact that the simplified numerical model fails to fully account for the localized interfacial polarization induced by nano-BTO within the time-varying multiphase grout system, as well as the reduced propagation loss resulting from the continuous decline in electrical conductivity during hydration.

Furthermore, the microstructural analysis provides a mechanistic explanation for the observed macroscopic dielectric constant variations. Nano-BTO particles are uniformly dispersed within the C-S-H gel matrix and ettringite-rich hydration products without forming obvious large-scale agglomerates. This uniform dispersion maximizes the interfacial contact area between BTO particles and surrounding hydration products, thereby providing abundant polarization centers that enhance interfacial polarization under high-frequency electromagnetic excitation. Concurrently, the physical shielding effect of fine BTO particles around cement grains and hydration products restricts water diffusion toward unhydrated cores. This microstructural barrier effect accounts for the delayed hydration process and the sustained decline in dielectric constant during the 24 h hydration period.

In practical underground engineering applications, the proposed nano-BTO active tracing technology can be effectively implemented through the following operational framework: First, in terms of on-site mixing, nano-BTO powder can be pre-dispersed into mixing water containing superplasticizers using industrial mixers prior to batching with cement, ensuring high suspension stability and preventing pipeline clogging during pressurized grouting. Second, to balance detection clarity with economic feasibility, a ‘boundary-pulse’ grouting protocol is recommended: standard neat cement grout can be injected during the primary bulk-filling phase, whereas BTO-modified grout (5–10% dosage) is injected specifically at the initial penetration stage or the terminal sealing phase to serve as an active

electromagnetic marker layer, sharply defining the outer boundary of grout diffusion without excessive material expenditure. Additionally, in practical cavity-filling or water-sealing operations, grouting essentially represents a dynamic process of displacing groundwater or void space with slurry. Elevating the grout permittivity via nano-BTO helps enhance the electromagnetic impedance mismatch against both the host rock and saturated voids, providing a viable physical basis for boundary delineation.

Overall, the experimental and numerical findings demonstrate that the proposed active electromagnetic tracing strategy—using high-dielectric nano-BTO to actively regulate the electromagnetic properties of cement grout—provides a viable and effective method to overcome the weak dielectric contrast inherent in conventional passive GPR detection. However, certain practical limitations of this methodology should be noted. First, the rheology, diffusion, and pumpability of BTO-modified grout within complex in situ fracture networks require further engineering-scale verification. Second, as an exploratory proof-of-concept study based on an idealized rock-grout interface and macroscopic effective permittivity inversion, future investigations should incorporate broadband complex permittivity spectroscopy and in situ fractured models to further examine interfacial polarization kinetics under complex hydrogeological conditions.

5. Conclusions

This study investigated an active electromagnetic tracing method for GPR based on nano-barium titanate (BTO) high-dielectric admixtures. Combined with continuous time-lapse GPR physical experiments and FDTD numerical simulations, the main conclusions are summarized as follows:

(1) SEM microstructural characterization confirmed that 100 nm BTO particles uniformly disperse within the C-S-H gel and ettringite networks without macro-agglomerations. This configuration maximizes rock-grout interfacial polarization sites to enhance dielectric response, while physically shielding unhydrated cement particles to retard hydration and prolong boundary detectability.

(2) Transforming the detection regime from passive sensing to active electromagnetic tracing via high-dielectric nano-BTO admixtures is a highly viable and effective strategy for overcoming the weak dielectric contrast in complex underground engineering. The incorporation of nano-BTO actively elevates the grout's dielectric constant and amplifies the electromagnetic impedance mismatch at the rock-grout interface, substantially boosting GPR reflection energy and boundary clarity. Concurrently, the nano-BTO particles exert a retarding effect on the early hydration process by acting as barriers that slow down water diffusion, thereby maintaining a sustained high electromagnetic response within the grout system and securing an extended time window for non-destructive inspection.

(3) Nano-BTO significantly alters the baseline magnitude and temporal evolution kinetics of the dielectric constant during hydration. The inclusion of 5% and 10% BTO increases the initial dielectric constant from 22.14 to 42.90 (an increase of 93.77%) and 49.70 (an increase of 124.48%), respectively. At the 24 h final node, while the pure cement grout reduces by 24.48% to a value of 16.72, the 5% and 10% BTO groups transition to values of 24.06 and 35.52, which represent a net dielectric advantage of 43.90% and 112.44%, respectively. Sample variance analysis confirms this transition from rapid convergence to a gradual decline, showing global peaks of 16.159 (5% BTO) and 11.350 (10% BTO) during the 400–1200 min interval.

(4) The incorporation of BTO significantly increases the interface reflection amplitude during both the initial and terminal stages of cement hydration. In laboratory physical experiments, compared with the pure cement control group, the initial reflection

amplitude increased by 36.66% (5% BTO) and 46.21% (10% BTO), respectively; at the 24 h node, the interface amplitudes of the cement grouts with 5% and 10% BTO dosages maintained high-level enhancements of 40.54% and 51.00%, respectively, compared to the pure cement grout at the same time node. The gprMax 3D numerical simulations present a similar trend, where the initial simulated amplitude enhancements for the 5% and 10% dosages are 39.95% and 47.48%, respectively, and the simulated enhancements at the 24 h node are 24.95% and 53.46%, respectively.

Author Contributions: Conceptualization, X.X., L.W. and Y.H.; methodology, R.T.; software, Z.Y.; validation, X.X., L.W. and Y.H.; data curation, R.T. and Z.Y.; writing—original draft preparation, X.X.; writing—review and editing, L.W.; project administration, R.T. All authors have read and agreed to the published version of the manuscript.

Funding: This research was funded by the Scientific Research Plan Project of Sinohydro Bureau 14 Corporation Limited under the project "Research on Key Technologies for Intelligent and Green Construction of Super-Large Caverns in Plateau Ecologically Fragile Areas" (Grant No. BDa-2025-KY01); State Key Laboratory of Geohazard Prevention and Geoenvironment Protection Independent Research Project "GPR Response Feature Quantification of Moraine Dam Structure for Real-time Monitoring and Early Warning" (Grant No. SKLGP2023Z018).

Data Availability Statement: The original contributions presented in this study are included in the article. Further inquiries can be directed to the corresponding author.

Acknowledgments: The authors would like to thank the laboratory technicians and staff for their assistance with the continuous GPR scanning equipment setup and the preparation of the cement grout specimens.

Conflicts of Interest: Authors Xianqi Xu and Zongren Yin were employed by the company Sinohydro Bureau 14 Co., Ltd. Author Rongping Tang was employed by the company Huaneng Lancang River Upper Stream Hydropower Co., Ltd., Banda Hydropower Project Construction Management Bureau. The remaining authors declare that the research was conducted in the absence of any commercial or financial relationships that could be construed as potential conflicts of interest.

References

1. Zhu, C.; Fu, J.; Wang, H.; Xia, Y.; Yang, J.; Wang, S. A Review of Grout Diffusion Mechanisms and Quality Assessment Techniques for Backfill Grouting in Shield Tunnels. *Buildings* **2026**, *16*, 97. [CrossRef]
2. Ma, J.; Sun, A.; Jiang, A.; Guo, N.; Liu, X.; Song, J.; Liu, T. Pressure Model Study on Synchronous Grouting in Shield Tunnels Considering the Temporal Variation in Grout Viscosity. *Appl. Sci.* **2023**, *13*, 10437. [CrossRef]
3. Jin, Y.; Yang, S.; Guo, H.; Han, L.; Huang, P.; Chen, M.; Shan, H.; Huang, L.; Su, S.; Wang, S.; et al. Dynamic Mechanical and Failure Properties of Grouted Fractured Rock Based on Nano-Grouting Material. *Processes* **2025**, *13*, 765. [CrossRef]
4. Hua, T.; Liu, S.; Zhang, X.; Meng, L.; Wang, P. Numerical Analysis of Grouting of Water-Enriched Karst Highway Tunnel Based on Critical Water-Enriched Height. *Processes* **2023**, *11*, 149. [CrossRef]
5. Du, X.; Li, Z.; Fang, H.; Li, B.; Zhao, X.; Zhai, K.; Xue, B.; Wang, S. A State-of-the-Art Review on the Study of the Diffusion Mechanism of Fissure Grouting. *Appl. Sci.* **2024**, *14*, 2540. [CrossRef]
6. Sun, F.; Fang, Q.; Li, P.; Pan, R.; Zhu, X. Research on the Water Inrush Mechanism and Grouting Reinforcement of a Weathered Trough in a Submarine Tunnel. *Buildings* **2024**, *14*, 2432. [CrossRef]
7. Gao, X.; Han, G.; Xue, X.; Liu, D.; Wang, Z.; Wei, C.; Yuan, S. Numerical Simulation of Grout Diffusion and Overlap Characteristics in Horizontal Curtain Grouting for Underground Mines Within 3D Discrete Fracture Networks. *Water* **2026**, *18*, 1669. [CrossRef]
8. Huang, Y.; Yang, W.; Li, Y.; Guo, W. Spatial Distribution Characteristics of Plastic Failure and Grouting Diffusion within Deep Roadway Surrounding Rock under Three-Dimensional Unequal Ground Stress and Its Application. *Minerals* **2022**, *12*, 296. [CrossRef]
9. Ma, R.; Jiang, W.; Lv, A.; Zhang, X.; Zhou, X.; Xie, X. Research and Application of Non-Destructive Inspection Technology For Backfill Grouting Quality Behind TBM and Shield Tunnel Segments. *Yellow River* **2021**, *43*, 139–143. [CrossRef]
10. Liu, H.; Yue, Y.; Lai, S.; Meng, X.; Du, Y.; Cui, J.; Spencer, B.F. Evaluation of the Antenna Parameters for Inspection of Hidden Defects Behind a Reinforced Shield Tunnel Using Gpr. *Tunn. Undergr. Space Technol.* **2023**, *140*, 105265. [CrossRef]

11. Wu, Y.; Wang, Y.; Li, D.; Zhang, J. Two-Step Detection of Concrete Internal Condition Using Array Ultrasound and Deep Learning. *NDT E Int*. **2023**, *139*, 102945. [CrossRef]
12. Ye, Z.; Ye, Y. Comparison of Detection Effect of Cavities Behind Shield Tunnel Segment Using Transient Electromagnetic Radar and Ground Penetration Radar. *Geotech. Geol. Eng*. **2019**, *37*, 4391–4403. [CrossRef]
13. Ran, M.; Zhou, X.; Yan, Y.; Jiang, R.; Zhou, X. Grouting Mechanism of Polyurethane Composite Materials in Asphalt Pavement Subsidence. *Materials* **2023**, *16*, 7052. [CrossRef] [PubMed]
14. Zhu, Z.; Zhao, S.; Qin, X.; Wu, H.; Zhao, C.; Wu, X. Model and Field Tests on Detection Effects of Tunnel Lining Cavity by Gpr. *Chin. J. Geotech. Eng*. **2022**, *44*, 132–137. [CrossRef]
15. Li, Q.; Lin, Z.; Pei, F.; Wang, C.; Shan, J.; Sun, P. Subgrade Grouting Test and Simulation Analysis. *Sci. Technol. Eng*. **2022**, *22*, 9339–9345. [CrossRef]
16. Tian, C.; Zeng, L.; Huang, Z.; Xie, X.; Wang, B.; Zeng, S. Real-Time Detection Technology for Shield Tunnel Synchronous Grouting and Grouting Effect Analysis. *Urban Mass Transit* **2020**, *23*, 124–128. [CrossRef]
17. Xie, X.; Zeng, L.; Zhou, B. Real-Time Detection Technology of Synchronous Grouting for Shield Tunnel and Analysis of Grouting Effect. In Proceedings of the 17th International Conference on Ground Penetrating Radar, GPR 2018, Rapperswil, Switzerland, 18–21 June 2018. [CrossRef]
18. Li, K.; Xie, X.; Zhou, B.; Zeng, L.; Huang, F. Cloud-Edge-End Architecture and Application for Intelligent Detection of Backfill Grouting in Shield Tunnels. *J. Civ. Environ. Eng*. **2025**, *47*, 67–76. [CrossRef]
19. Peng, M.; Wang, D.; Liu, L.; Shi, Z.; Shen, J.; Ma, F. Recent Advances in the GPR Detection of Grouting Defects behind Shield Tunnel Segments. *Remote Sens*. **2021**, *13*, 4596. [CrossRef]
20. Mohajerani, A.; Burnett, L.; Smith, J.V.; Kurmus, H.; Milas, J.; Arulrajah, A.; Horpibulsuk, S.; Abdul Kadir, A. Nanoparticles in Construction Materials and Other Applications, and Implications of Nanoparticle Use. *Materials* **2019**, *12*, 3052. [CrossRef] [PubMed]
21. Huang, T.; Xu, H.; Zhao, Y.; Xu, F.; Xu, K.; Feng, Z.; Deng, Z.; Zhu, G. Study on the Preparation and Properties of Nano-Sized Barium Titanate Slurry and Tape Casting. *J. Funct. Mater.* **2024**, *11*, 11084–11089. [CrossRef]
22. Zhang, P.; Wang, X.; Li, Z. Research Progress in piezoelectric catalysis of Barium Titanate Nanomaterials. *Acta Mater. Compos. Sin*. **2023**, *40*, 1285–1299. [CrossRef]
23. Akyıldız, A.; Balcan, B. The Electromagnetic and Mechanical Properties of Barium Titanate Nanopowder Additive Cement Based Composite. *Fuller. Nanotub. Carbon Nanostruct*. **2025**, *34*, 54–61. [CrossRef]
24. Ctibor, P.; Straka, L.; Lukáč, F.; Sedláček, J. Stability Study of Dielectric Properties of Plasma-Sprayed BaTiO3. *Coatings* **2022**, *12*, 355. [CrossRef]
25. Wang, L.; Wang, X.; Wu, Y.; Ma, Y.; Sun, X.; Zhang, S.; Xu, Y.; Yuan, Y.; Li, Y. Preparation and Wave-Absorbing Properties of Batio3/Carbon nanofiber Mesh Composite Wave-Absorbing Fabric. *J. Aeronaut. Mater.* **2024**, *44*, 187–195. [CrossRef]
26. Li, J.; Liu, L.; Shen, Z.; Xu, T.; Zhou, Z. Design, Preparation and electromagnetic Properties of Lightweight multilayer absorbing Materials. *J. Funct. Mater.* **2021**, *52*, 11001–11008. [CrossRef]
27. Wittinanon, T.; Rianyoi, R.; Potong, R.; Pan, H.H.; Chaipanich, A. Effect of Epoxy Resin and Barium Zirconate Titanate Contents on the Piezoelectric Properties of a 0–3 Barium Zirconate Titanate-Portland Cement Composite with Epoxy Resin Addition. *Ceram. Int*. **2023**, *49*, 18195–18202. [CrossRef]
28. Wittinanon, T.; Rianyoi, R.; Potong, R.; Chaipanich, A. Electromechanical Properties and Mechanical Quality Factor of 1–3 Connectivity Lead-Free Barium Zirconate Titanate Ceramic/Epoxy Resin Modified Cement-Based Composites. *Ceram. Int*. **2025**, *51*, 22932–22941. [CrossRef]
29. Wittinanon, T.; Rianyoi, R.; Chaipanich, A. Electromechanical Properties of Barium Titanate-Polyvinylidene Fluoride Cement-Based Composites. *Constr. Build. Mater.* **2021**, *299*, 123908. [CrossRef]
30. S, S.M.; Kattimani, S.; Saminathan, R. Effect of Bto Piezoceramic on the Mechanical and Dielectric Properties of 3d-Printed Pla.Bto Functional Polymer Composite. *Emergent Mater.* **2025**, *8*, 6719–6746. [CrossRef]
31. Ye, J.; Zhang, B.; Jin, Y.; Zhang, H.; Qiao, Y.; Zhang, Z. 3d Segregated Architecture Batio3/Polystyrene Composites with Enhanced Dielectric Constant Fabricated Via Hot Pressing Core–Shell Polystyrene@Batio3 Composite Microspheres. *J. Mater. Sci. Mater. Electron*. **2020**, *31*, 3101–3110. [CrossRef]
32. Xie, L.; Xia, Z.; Xue, S.; Fu, X. Detection of Setting Time during Cement Hydration Using Ground Penetrating Radar. *J. Build. Eng*. **2022**, *60*, 105166. [CrossRef]
33. He, R.; Lu, N. Unveiling the Dielectric Property Change of Concrete during Hardening Process by Ground Penetrating Radar with the Antenna Frequency of 1.6 ghz and 2.6 ghz. *Cem. Concr. Compos*. **2023**, *144*, 105279. [CrossRef]
34. Oikonomopoulou, E.C.; Palieraki, V.A.; Sfikas, I.P.; Trezos, C.G. Reliability and Limitations of Gpr for Identifying Objects Embedded in Concrete—Experience from the Lab. *Case Stud. Constr. Mater.* **2022**, *16*, e00898. [CrossRef]
35. Zhai, J.; Wang, Q.; Wang, H.; Xie, X.; Zhou, M.; Yuan, D.; Zhang, W. Highway Tunnel Defect Detection Based on Mobile GPR Scanning. *Appl. Sci*. **2022**, *12*, 3148. [CrossRef]

36. Ling, T.; He, W.; Zhang, S.; Liu, X.; Huang, F.; Liu, W. A New Method for Measuring the Relative Dielectric Constant of Porous Mixed Media Using Gpr, and Its Application. *Constr. Build. Mater.* **2022**, *353*, 129042. [CrossRef]
37. Taylor, J.M.; Morris, I.M. Investigating Concrete Properties Using Dielectric Constant from Ground Penetrating Radar Scans. *Infrastructures* **2022**, *7*, 173. [CrossRef]
38. Shen, J.; Liang, R.; Jia, L.; Yu, W.; Zheng, Q. Synergistically Enhance Toughness and Electrical Breakdown Resistance of Polypropylene by B-Crystal Modification. *Acta Polym. Sin.* **2026**, *57*, 595–607. [CrossRef]
39. Li, K.; Xie, X.; Zhou, B.; Huang, F.; Zhou, Y.; Li, M. Model Test Study on Gpr Detection for Cement-Sodium Silicate Synchronous Grouting in Shield Tunnel. *China J. Highw. Transp.* **2024**, *37*, 330–341. [CrossRef]
40. Izadi-Yazdanabadi, M.; Hojat, A.; Zanzi, L.; Karimi-Nasab, S.; Arosio, D. Analytical Models and Laboratory Measurements to Explore the Potential of GPR for Quality Control of Marble Block Repair through Resin Injections. *Appl. Sci.* **2022**, *12*, 987. [CrossRef]
41. Zanzi, L.; Izadi-Yazdanabadi, M.; Karimi-Nasab, S.; Arosio, D.; Hojat, A. Time-Lapse GPR Measurements to Monitor Resin Injection in Fractures of Marble Blocks. *Sensors* **2023**, *23*, 8490. [CrossRef]
42. Warren, C.; Giannopoulos, A.; Giannakis, I. Gprmax: Open Source Software to Simulate Electromagnetic Wave Propagation for Ground Penetrating Radar. *Comput. Phys. Commun.* **2016**, *209*, 163–170. [CrossRef]
43. Liu, H.; Huo, Y.; Yi, L. Three-Dimensional Quantitative Forward Modeling of Obstacles and Detected Objects at Different Distances in Air-Coupled Ground-Penetrating Radar. *Sci. Technol. Eng.* **2025**, *25*, 6189–6199. [CrossRef]

Disclaimer/Publisher's Note: The statements, opinions and data contained in all publications are solely those of the individual author(s) and contributor(s) and not of MDPI and/or the editor(s). MDPI and/or the editor(s) disclaim responsibility for any injury to people or property resulting from any ideas, methods, instructions or products referred to in the content.